

The British University in Egypt

BUE Scholar

Mechanical Engineering

Engineering

2024

Photoexcited Charge Carrier Dynamics and Electronic Properties of Two-dimensional MXene, Nb₂CTx

Andrew M. Fitzgerald

Department of Physics, Worcester Polytechnic Institute, Worcester, MA, USA

Emily Sutherland

Department of Physics, Worcester Polytechnic Institute, Worcester, MA, USA

Tarek A. Elmelegy

The British University in Egypt, tarek.elmelegy@bue.edu.eg

Mary Qin Hassig

Department of Materials Science and Engineering, Drexel University, Philadelphia, PA, USA

Julia Martin

Department of Chemistry and Biochemistry, Worcester Polytechnic Institute, Worcester, MA, USA

See next page for additional authors

Follow this and additional works at: https://buescholar.bue.edu.eg/mech_eng



Part of the [Ceramic Materials Commons](#), [Nanoscience and Nanotechnology Commons](#), and the [Semiconductor and Optical Materials Commons](#)

Recommended Citation

Fitzgerald, Andrew M.; Sutherland, Emily; Elmelegy, Tarek A.; Hassig, Mary Qin; Martin, Julia; Colin-Ulloa, Erika; Ngo, Ken; L. Grimm, Ronald; Uzarski, Joshua R.; Barsoum, Michel W.; Deskins, N. Aaron; Titova, Lyubov V.; and Friedman, Kateryna Kushnir, "Photoexcited Charge Carrier Dynamics and Electronic Properties of Two-dimensional MXene, Nb₂CTx" (2024). *Mechanical Engineering*. 69.

https://buescholar.bue.edu.eg/mech_eng/69

This Article is brought to you for free and open access by the Engineering at BUE Scholar. It has been accepted for inclusion in Mechanical Engineering by an authorized administrator of BUE Scholar. For more information, please contact bue.scholar@gmail.com.

Authors

Andrew M. Fitzgerald, Emily Sutherland, Tarek A. Elmelegy, Mary Qin Hassig, Julia Martin, Erika Colin-Ulloa, Ken Ngo, Ronald L. Grimm, Joshua R. Uzarski, Michel W. Barsoum, N. Aaron Deskins, Lyubov V. Titova, and Kateryna Kushnir Friedman

ACCEPTED MANUSCRIPT

Photoexcited charge carrier dynamics and electronic properties of two-dimensional MXene, Nb₂CT_x

To cite this article before publication: Andrew M. Fitzgerald *et al* 2024 *2D Mater.* in press <https://doi.org/10.1088/2053-1583/ad518d>

Manuscript version: Accepted Manuscript

Accepted Manuscript is “the version of the article accepted for publication including all changes made as a result of the peer review process, and which may also include the addition to the article by IOP Publishing of a header, an article ID, a cover sheet and/or an ‘Accepted Manuscript’ watermark, but excluding any other editing, typesetting or other changes made by IOP Publishing and/or its licensors”

This Accepted Manuscript is © 2024 IOP Publishing Ltd.



During the embargo period (the 12 month period from the publication of the Version of Record of this article), the Accepted Manuscript is fully protected by copyright and cannot be reused or reposted elsewhere.

As the Version of Record of this article is going to be / has been published on a subscription basis, this Accepted Manuscript will be available for reuse under a CC BY-NC-ND 3.0 licence after the 12 month embargo period.

After the embargo period, everyone is permitted to use copy and redistribute this article for non-commercial purposes only, provided that they adhere to all the terms of the licence <https://creativecommons.org/licenses/by-nc-nd/3.0>

Although reasonable endeavours have been taken to obtain all necessary permissions from third parties to include their copyrighted content within this article, their full citation and copyright line may not be present in this Accepted Manuscript version. Before using any content from this article, please refer to the Version of Record on IOPscience once published for full citation and copyright details, as permissions may be required. All third party content is fully copyright protected, unless specifically stated otherwise in the figure caption in the Version of Record.

View the [article online](#) for updates and enhancements.

Photoexcited Charge Carrier Dynamics and Electronic Properties of Two-dimensional MXene, Nb₂CT_x

Andrew M. Fitzgerald^{1&}, Emily Sutherland^{1&}, Tarek Ali El-Melegy^{2,3}, Mary Qin Hassig³, Julia Martin⁴, Erika Colin-Ulloa¹, Ken Ngo⁵, Ronald L. Grimm⁴, Joshua R. Uzarski⁵, Michel W. Barsoum³, N. Aaron Deskins⁶, Lyubov V. Titova^{1*}, and Kateryna Kushnir Friedman^{1*}

¹ Department of Physics, Worcester Polytechnic Institute, Worcester, MA, USA

² Department of Mechanical Engineering, The British University in Egypt, Cairo, Egypt

³ Department of Materials Science and Engineering, Drexel University, Philadelphia, PA, USA

⁴ Department of Chemistry and Biochemistry, Worcester Polytechnic Institute, Worcester, MA, USA

⁵ US Army DEVCOM Soldier Center, Natick, MA, USA

⁶ Department of Chemical Engineering, Worcester Polytechnic Institute, Worcester, MA, USA

& Equal contribution

* ltitova@wpi.edu, kkushnir@wpi.edu

Abstract

Two-dimensional, 2D, niobium carbide MXene, Nb₂CT_x, has attracted attention due to its extraordinarily high photothermal conversion efficiency that has applications ranging from medicine, for tumor ablation, to solar energy conversion. Here, we characterize its electronic properties and investigate the ultrafast dynamics of its photoexcitations with a goal of shedding light onto the origins of its unique properties. Through density functional theory, DFT, calculations, we find that Nb₂CT_x is metallic, with a small but finite density of states at the Fermi level for all experimentally relevant terminations of Nb₂CT_x that can be achieved using HF or molten salt etching of the parent MAX phase, including -OH, -O, -F, -Cl, -Br, -I. In agreement with this prediction, THz spectroscopy reveals an intrinsic long-range conductivity of $\sim 60 \Omega^{-1} \text{cm}^{-1}$, with significant charge carrier localization and a charge carrier density ($\sim 10^{20} \text{cm}^{-3}$) comparable to Mo-based MXenes. Excitation with 800 nm pulses results in a rapid enhancement in photoconductivity, which decays to less than 25% of its peak value within several picoseconds, underlying the efficient photothermal conversion. At the same time, a small fraction of photoinjected excess carriers persists for hundreds of picoseconds, and can potentially be utilized in photocatalysis or other energy conversion applications.

Keywords: MXenes, 2D materials, Terahertz Spectroscopy, Density Functional Theory

1. Introduction

Discovered in 2011, MXenes are a class of two-dimensional, 2D, transition metal carbides, nitrides, and carbonitrides. These materials share the general chemical formula $M_{n+1}X_nT_x$, where M is an early transition metal, X is carbon or nitrogen, n takes on a value from 1 – 4, and T_x stands for the surface terminations, such as –OH, –O, or –F. The latter form when the A-layer, typically Al, is selectively etching away from their parent MAX-phases.^[1] Several different MXene materials have displayed exceptional properties, including high conductivity, record high volumetric capacitances, nonlinear optical effects, and efficient photothermal conversion, suggesting the potential for applications in electromagnetic interference shielding^[2-4], energy storage^[5-13], optoelectronic and photonic devices^[14-20], electrochemical sensors^[21, 22], and even photothermal cancer treatments^[23-27].

A member of MXene family, niobium carbide, Nb_2CT_x , was discovered in 2013,^[8] and has since been drawing attention for its high photothermal conversion efficiency^[23, 24, 28, 29], good biocompatibility^[23], high reversible capacity (when integrated into battery anodes or electrodes)^[8, 9, 11, 13], and nonlinear optical properties^[19, 20, 30], rendering this MXene potentially attractive for applications in photothermal cancer therapy, antibacterial sterilization, batteries, and optoelectronic and photonic devices. Despite numerous experimental and computational studies, the electronic properties of Nb_2CT_x with different surface terminations, the nature of conductivity and the behavior of photoexcitations in this MXene are not well described or characterized. For instance, unlike the highly conductive $Ti_3C_2T_x$, Ti_2CT_x , or V_2CT_x ^[18, 31], Nb-based MXenes such as Nb_2CT_x and $Nb_4C_3T_x$ have been reported to have low intrinsic electrical conductivities, raising the question of whether these MXenes possess a metallic or semiconducting nature.^[32] In our recent work, we demonstrated that Nb_2CT_x with mixed O and OH terminations exhibits a surface plasmon resonance despite having a low intrinsic free carrier density, pointing to its metallic nature.^[33]

In this study, we investigate the electrical and optical properties of Nb_2CT_x by combining Density Functional Theory (DFT) calculations of its electronic structure, as a function of surface terminations, with experimental measurements of intrinsic and photoexcited conductivities using terahertz (THz) spectroscopy. Recent DFT studies uncovered that the surface terminations, T_x , play a defining role in determining whether or not a small gap opens in the band structure of Nb-based MXenes.^[35, 36] Here, model Nb_2CT_x with a number of surface terminations. We study Nb_2CT_x with hydroxyl, oxygen, or a combination of these terminations that occur when it is fabricated by HF etch of the parent Nb_2AlC MAX phase followed by delamination in a NaOH, TMAOH or TBAOH^[8, 37, 38] which matches the film we use for experiments. In addition, we investigate $T_x=N$, which has previously been predicted to result in opening of a band gap^[35], as well as halogen terminations that result from etching of MAX phase using malted salts^[39-43]. We find that Nb_2CT_x is metallic for all surface terminations with the exception of nitrogen. In agreement with this, THz-TDS shows that Nb_2CT_x sheets have an intrinsic free carrier density on the order of 10^{20} cm^{-3} and considerable intra-sheet carrier mobility of $\sim 30 \text{ cm}^2 \text{ V}^{-1} \text{ s}^{-1}$, comparable to other MXenes.^[31, 44-46] Long-range transport in macroscopic films is limited by nanosheet boundaries that suppress the inter-sheet mobility more than ten-fold to $2.4 \pm 0.4 \text{ cm}^2 \text{ V}^{-1} \text{ s}^{-1}$. Finally, we find that photoexcitation transiently enhances Nb_2CT_x conductivity, as has been reported in other metallic MXenes with intrinsic carrier density $\sim 10^{20} \text{ cm}^{-3}$ or below, such as $Mo_2Ti_2C_3T_x$, $Mo_2TiC_2T_x$ or $Nb_4C_3T_x$, and in contrast to MXenes with high carrier density $> 10^{21} \text{ cm}^{-3}$, such as $Ti_3C_2T_x$, where conductivity is suppressed as rapid lattice heating results in lower carrier mobility.^[31, 32, 44-46] We find that most of the optically injected carriers recombine

and are trapped at the defect states within one picosecond after excitation, while a small fraction persists for tens and hundreds of picoseconds. Thus, ultrashort photoexcited carrier lifetime may be utilized in high-speed photoelectronic devices as another potential application of this MXene.

2. Methods

2.1 Synthesis

2.1.1 MAX Phase Synthesis

To synthesize the Nb_2AlC phase, first, powders of Nb (99.8% purity, 1-5 μm), Al (99.5% purity, < 44 μm , -325 mesh), and C (99% purity, < 48 μm , -300 mesh), all acquired from Alfa Aesar, were mixed in a 2:1.1:1 molar ratio in a polyethylene jar with zirconia milling balls, 5-20 mm in diameter. Excess Al compensates for evaporation and aluminothermic reduction of native metal oxides. The mixed powders were ball-milled (U.S Stoneware, OH, USA) for 24 h at 70 rpm and then transferred to an alumina, Al_2O_3 , boat, which was placed inside an Al_2O_3 tube furnace and heated under flowing argon, Ar, (flow rate 15 SCCM) to 1600 °C for 4 h at a heating rate of 3 °C/min. The resulting solid was then drilled into a powder and sieved through a 400 mesh to obtain a powder with a particle size of less than 38 μm .

2.1.2 Mxene Etching

Multilayered (ML) Nb_2CT_z flakes were obtained by etching 1 g of Nb_2AlC powder in 10 ml of HF solution (50 wt.%, Acros Organics, Morris Plains, USA) and stirring (PC-420D, Corning, NY, USA) for 96 h at 55 °C and 400 rpm. The resulting slurry was decanted into a 50 ml centrifuge tube, and deionized, DI, water (18 M Ω .cm, Milli-Q, Merck KgaA, Darmstadt, Germany) was added to fill the remaining volume. The centrifuge tube was then sealed and shaken for 60 s (Fisherbrand™ Analog Vortex Mixer, Hampton, NH, USA), after which it was centrifuged at 3500 rpm for 120 s (Sorvall ST 16, Thermo Fisher Scientific, MA, USA). The supernatant was discarded, then DI water was added, and washing was repeated until the pH of the supernatant reached ≈ 7 . After washing, the MXene-containing sediment was collected and air dried.

2.1.3 MXene Delamination

To delaminate the Nb_2CT_z MLs into single to few layers, ≈ 0.2 g of the ML from the washing process was dispersed in 2 mL of tetrabutylammonium hydroxide, TBAOH, (40 wt.% in water, Alfa Aesar, MA, USA) and shaken in for 15 min. The mixture was washed twice with ethanol (200-proof, Fisher Scientific, NH, USA), followed by a final DI water washing stage. After washing off excess TBAOH, the sediments were redispersed in fresh DI water, and the mixture was then sonicated (Model 505 Sonic Dismembrator, 500 W, Fisher Scientific, NH, USA) under bubbling Ar flow for 1 h with 30s/30s on/off cycles at 75% amplitude. To avoid oxidation, the bath temperature was maintained below 20 °C using ice. The solution was centrifuged for 1 h at 3500 rpm, the supernatant was decanted into a fresh centrifuge tube, while the residual sediment containing any unetched MAX or non-delaminated MXene was discarded.

2.1.4 Mxene Deposition

The resultant Nb₂CT_x colloid was deposited by a gravity-feed, compressed-gas-propelled commercial airbrush (Master Airbrush, G233) onto IR-grade quartz to produce a thin film of Nb₂CT_x. Spray depositions utilized ~0.25 mL of a 1:10 aqueous dilution of the concentrated Nb₂CT_x colloid. Routine cleaning of the airbrush body and components utilized dilute, aqueous glacial acetic acid (AcOH, 99.7%, Alfa Aesar). Components in frequent contact with Nb₂CT_x material including the needles, fluid tips, and reservoir were sonicated in the aqueous, dilute acetic acid and rinsed with copious amounts of water in between subsequent depositions. This process results in a multilayer film consisting of many individual nanoflakes with sub- μm lateral dimensions. In such films, the transport properties result from an interplay of short-range, intra-flake carrier motion and long-range, inter-flake hopping transport^[32, 45]. Using a stylus profilometer, we found the thickness of this Mxene film to be 185 ± 11 nm.

2.2 Density Functional Theory (DFT)

All DFT calculations were performed using the Vienna ab initio Simulation Package (VASP)^[47-50]. The generalized gradient approximation (GGA) exchange correlation functional by Perdew, Burke, and Ernzerhof (PBE)^[51] was utilized for our calculations. Projector augmented wave (PAW) pseudopotentials^[52, 53] described the core electron states. The cutoff energy for valence electron wavefunctions was set to 450 eV. The Brillouin zone was sampled with a Γ -centered mesh with $3 \times 3 \times 1$ k-points. During structure relaxation, calculation convergence criteria for energies and forces were set to 10^{-5} eV and 0.002 eV/Å, respectively. The Gaussian smearing method was used with a width 0.25 eV, which was chosen to optimize the smoothness of density of states (DOS) curves. To further confirm the metallic nature and or identify potential band gap, DOS calculations were performed using the HSE06 exchange correlation functional^[54] with a smearing width of 0.05 eV (recommended by the VASP documentation for semiconductors). Since HSE06 calculations are so time-consuming, we used the PBE geometries for the HSE06 calculations. Post-processing extraction of density of state values and band structure from VASP simulations was carried out using the VASPKIT package^[55].

We studied the electronic structure for 3×3 supercells of Nb₂CT₂ MXenes with T = O, F, OH, N, Cl, Br, and I. We modeled Nb₂CT₂ MXenes with mixed OH/O terminations in a 1:1 ratio, and mixed OH/F terminations in 1:1, 2:1 and 5:1 ratios. Previous literature suggests that mixed terminations may be randomly distributed and depend on the synthesis method.^[56-58] Accordingly, we modeled mixed termination MXenes also with random configurations, and having symmetry between the top and bottom surfaces maximized (see Figure S5). MXenes generally have trigonal symmetry with terminations located either in the hollow sites above metal atoms (h_M) as in Figure 1(a, b), or in the hollow sites above X (carbon or nitrogen) atoms (h_X) as in Figure 1(c, d). Sample calculations for Nb₂CF₂, and Nb₂C(OH)₂, predict these structures to have an energetic preference for the h_M configuration, which is consistent with the most stable configuration predicted for Nb₂CT₂ in other studies^[59, 60]. Therefore, in this work all structures were modeled with trigonal symmetry and the h_M termination configuration. To avoid interlayer interactions, the cell length along the z direction was set to 20 Å.

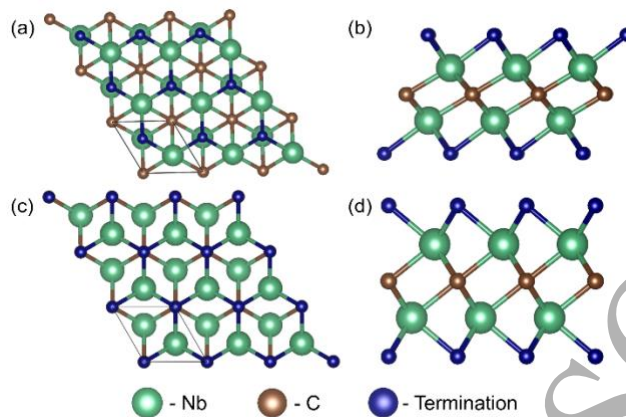


Figure 1. Top (left) and side (right) views of Nb_2CT_2 MXenes modeled in this work. The h_M configuration is shown in (a, b) and the h_X configuration is shown in (c, d). Green spheres are Nb atoms, brown spheres are carbon, and blue spheres are representative of terminations. The diamond outline shown in the top view outlines a single unit cell. Figures for all modeled structures are given in Supporting Information, SI.

2.3 Terahertz Spectroscopy

The intrinsic conductivity of Nb_2CT_x in the 0.25 – 2.5 THz range was investigated using THz time-domain Spectroscopy (THz-TDS) in transmission mode^[31, 45, 61-63]. THz-TDS is a non-contact, all-optical technique that allows measurement of complex, frequency-resolved conductivity. THz probe pulses were generated in a 1 mm-thick ZnTe [100] crystal upon photoexcitation with 800 nm, 100 fs pulses from an amplified Ti: Sapphire laser. The bandwidth of the generated THz pulses spans in the 1-10 meV range. Off-axis parabolic mirrors were used to focus THz pulses onto the ~ 1.5 mm spot on the sample at normal incidence and to collect transmitted THz pulses, directing them to the detector. They were detected in another 1mm – thick [100] ZnTe crystal using electro-optic sampling. Analyzing the amplitude and phase of the THz pulse through the substrate and sample in the frequency domain yields the complex frequency-resolved conductivity of the material.^[64, 65]

In addition, time-resolved THz spectroscopy (TRTS) was used to study the effects of photoexcitation with 800 nm (1.55 eV), 100 fs pulses.^[61, 66-69] The optical excitation beam was directed to the sample through a 5 mm aperture in the parabolic mirror that focused the THz probe pulse onto the sample. A larger optical excitation spot size (≈ 5 mm) ensured uniform illumination of the entire THz probe pulse spot on the MXene sample. A mechanical delay line was used to control the arrival time of the THz probe pulse relative to the optical excitation pulse.

3. Results and Discussion

3.1 Density Functional Theory (DFT)

Earlier studies on Nb_2CT_x have reported a negligibly low conductivity for this MXene,^[18] leading to the hypotheses

1
2
3 that Nb-based MXenes may be semiconducting rather than metallic in nature. However, observed plasmonic properties
4 suggest the presence of a nonzero, and measurable, concentration of free charge carriers.^[33] Accordingly, we used
5 DFT to model electronic properties of Nb₂CT₂ MXenes in order to establish the nature of the conductivity of these
6 materials.
7

8
9 Initial band structure and density of state (DOS) calculations, using the PBE functional, revealed a metallic nature
10 for bare Nb₂C, which is retained upon adsorption of O, F, OH, Cl, Br, and I groups (see Figure 2). Further DOS
11 calculations using the HSE06 functional, which is known to be more accurate than PBE for predicting conductive
12 nature, confirm that these MXenes are metals (see SI for figures). Our results are in agreement with literature.^{[36, 59, 60,}
13 ^{70, 71]} Additionally, our simulations of Nb₂CT₂ with mixed OH/F and O/OH terminations indicate that the metallic
14 nature is also preserved when multiple termination types are present, independent of their ratio (see SI for Figures S6
15 and S7). In the case of nitrogen, N, terminations, however, Nb₂CT_x transitions to a semiconductor with a band gap of
16 0.25 eV with PBE and 0.66 eV with HSE06, which is in agreement with previous studies.^[35, 72, 73] The band gap may
17 be difficult to see in the DOS due to the smearing applied to the DOS. However, the band gap in Nb₂CN₂ is evident
18 from the band structure (Figure 2), as well as examining the energy eigenvalues in the OUTCAR file.

19
20 Partial density of states, PDOS, curves for Nb₂CT₂, shown in Figure 2 and SI, reveal that the electronic states of
21 Nb atoms dominate the electronic structure near the Fermi level, E_F, while the C, F, O, Cl, Br and H atoms have much
22 less contribution. This indicates that the d-orbitals of Nb atoms are responsible for the metallic nature of Nb₂CT_x with
23 Cl, Br, O, F, and/or OH terminations. For Nb₂CN₂, however, Nb-N bonding produces a shift in the E_F such that a band
24 gap is opened. Nb₂Cl₂ has significant contributions from both Nb and I atoms at E_f, indicating that this material may
25 have notably higher electrical conductivity as compared to the other Nb₂CT₂ MXenes considered in this study.
26 MXenes with Cl, Br, or I terminations are rare, however, as they are typically synthesized using molten salts.^[39-43]
27 Future studies may examine this material in detail.

28
29 As previously reported for Nb₂CT_x synthesized as described above, X-ray photoelectron spectroscopy (XPS) shows
30 that Nb₂CT_x has much more surface oxides than Ti₃C₂T_x or Mo₂Ti₂C₃T_x, and the only terminations present are O and
31 OH. No measurable F was detected, probably due to the removal of fluorine during TBAOH treatment.^[37] The exact
32 Nb:C ratio, considering only the components ascribed to MXenes, was found to be 2:0.9. As no F was detected, the
33 chemical formula derived using XPS is Nb₂C_{0.9}(O/OH)₂. As noted above, for the O and OH terminations, DFT
34 unambiguously predicts the metallic nature of Nb₂CT_x.
35
36
37
38
39
40
41
42
43
44
45
46
47
48
49
50
51
52
53
54
55
56
57
58
59
60

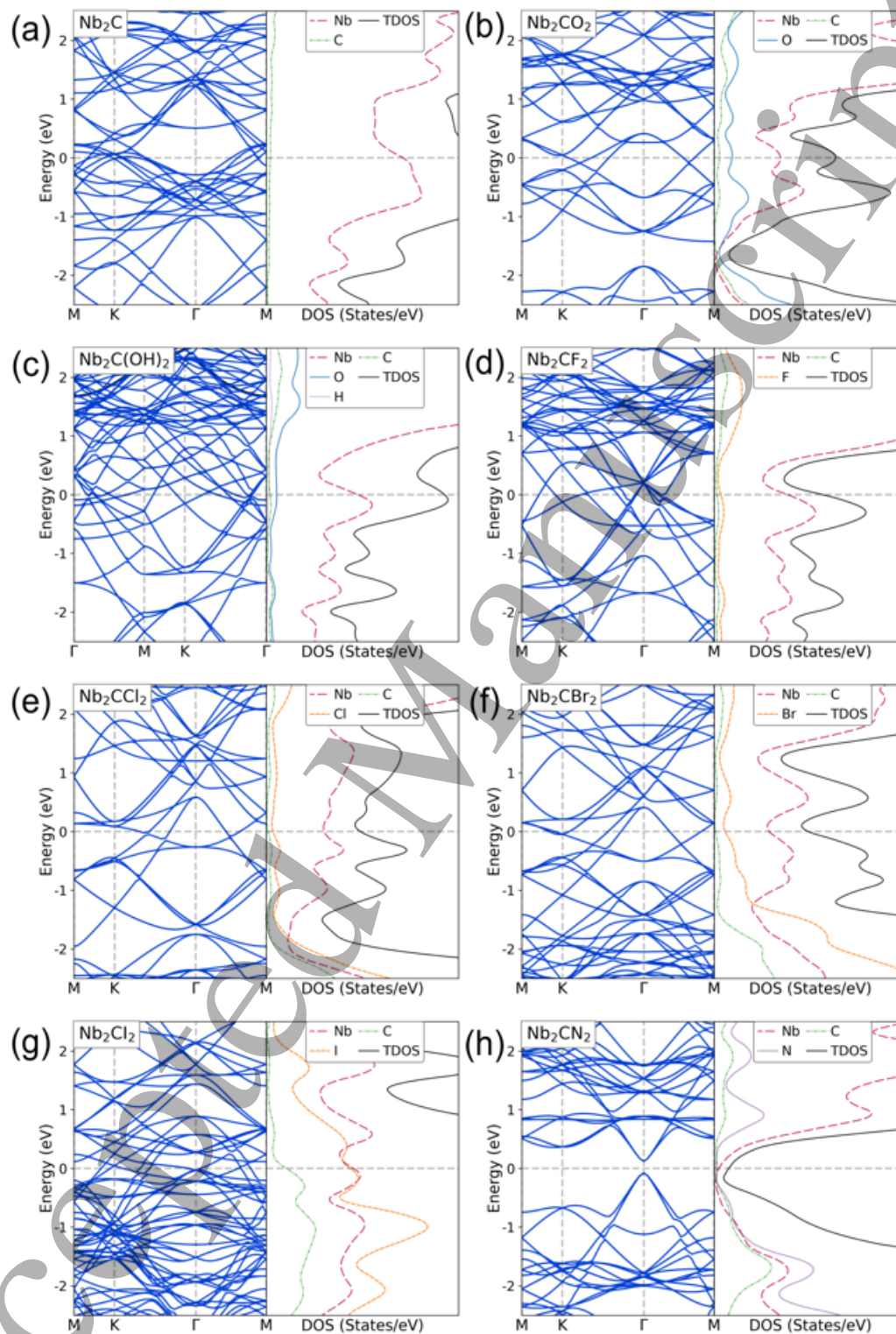


Figure 2. Band structure and DOS plots for Nb_2C (a), Nb_2CO_2 (b), $\text{Nb}_2\text{C}(\text{OH})_2$ (c), Nb_2CF_2 (d), Nb_2CCl_2 (e), Nb_2CBr_2 (f), Nb_2Cl_2 (g), and Nb_2CN_2 (h) as calculated by DFT using the PBE exchange correlation functional. These results predict Nb_2CN_2 to be semiconducting, and all others to be metallic. All DOS plots are scaled identically. Energies are shown relative to the Fermi energy (0 eV).

3.2 THz Time-domain Spectroscopy (THz-TDS)

Figure 3(a) shows the THz pulses transmitted through the quartz substrate alone and through the 185 ± 11 nm thick Nb_2CT_x film deposited on top of the quartz substrate. The inset shows the amplitude spectra of the same THz pulses in the frequency domain. The frequency-dependent, complex conductivity of Nb_2CT_x can be calculated from the amplitude and phase of the THz pulses that have been transmitted through the sample on the quartz substrate and through the quartz substrate alone using

$$\frac{\tilde{E}_{\text{sample}}(\omega)}{\tilde{E}_{\text{substrate}}(\omega)} = \frac{n+1}{n+1+Z_0\tilde{\sigma}(\omega)}, \quad (1)$$

where n is the refractive index of the quartz substrate in the THz frequency range (~ 2.156 , assumed here to be constant as reported variation is $<1\%$ within the 0.25-2.5 THz range)^[74], Z_0 is the impedance of free space (377Ω), and $\tilde{E}_{\text{sample}}(\omega)$ and $\tilde{E}_{\text{substrate}}(\omega)$ are the electric fields of the THz pulses transmitted through the sample and substrate together and through the substrate alone.^[31, 61, 75]

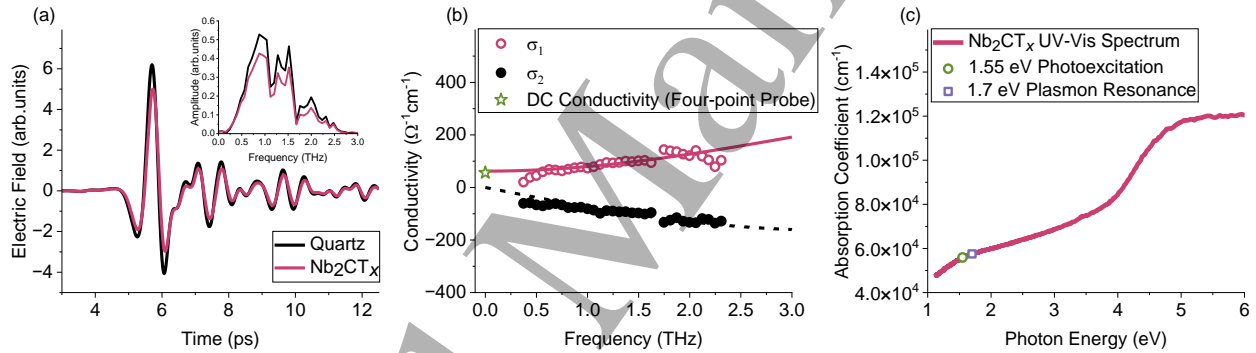


Figure 3. (a) THz waveforms in the time-domain transmitted through quartz (black) alone and through a thin-film sample of Nb_2CT_x deposited onto the quartz substrate. Inset plots THz amplitude in the frequency-domain. (b) Real (σ_1) and imaginary (σ_2) intrinsic conductivities of Nb_2CT_x . Lines represent fits to the Drude-Smith model for complex conductivity (solid line – fit to real part of model; dashed line – fit to imaginary part of model). Green star represents DC conductivity measured by four-point probe. Experimental error on this measurement is smaller than the symbol size. (c) Optical absorption coefficient of Nb_2CT_x in UV-near IR spectral range. Photon energy used in TRTS measurements (1.55 eV) is shown as an open circle. Also shown is a center photon energy of a plasmon resonance reported earlier in Nb_2CT_x [Ref.29], 1.7 eV.

Figure 3(b) plots the real (σ_1) and imaginary (σ_2) parts of this intrinsic conductivity as functions of frequency. To model the complex conductivity, we employ the Drude-Smith model, a modification of the free carrier Drude conductivity that incorporates the effects of carrier localization over distances comparable to their mean free path by the disorder and grain boundaries or, in this case, the boundaries of individual Nb_2CT_x nanosheets.^[45, 62, 76-78]

The Drude-Smith model for complex conductivity is given by

$$\tilde{\sigma}(\omega) = \frac{\sigma_0}{1-i\omega\tau_{DS}} \left(1 + \frac{c}{1-i\omega\tau_{DS}} \right), \quad (2)$$

where c is the localization parameter, τ_{DS} is carrier scattering time, and σ_0 is given by

$$\sigma_0 = \frac{Ne^2\tau_{DS}}{m^*}, \quad (3)$$

where N is the intrinsic charge carrier density and m^* is the carrier effective mass.^[45, 79] In the Drude-Smith model, the localization parameter can take on a value between 0 and -1. For $c = 0$, charge carriers move throughout a sample entirely unimpeded; for $c = -1$, the charge carriers' movement is entirely suppressed or localized.

Lines in Fig. 3(b) represent the global fit of both real and imaginary intrinsic conductivity to Eq. 2

Note that the complexity of the Fermi surface in Nb_2CT_x , that can be inferred from the band structure diagrams in Fig. S8, complicates calculation of the effective carrier mass necessary for extracting the carrier density from the Drude-Smith fitting parameters. For the sake of obtaining an estimate of Nb_2CT_x carrier density, we assume here $m^* = m_e$, and in doing so, we find that $N = (1.6 \pm 0.3) \times 10^{20} \text{ cm}^{-3}$.

The charge carrier density we find here is comparable to that of $\text{Mo}_2\text{Ti}_2\text{C}_3\text{T}_x$ and $\text{Mo}_2\text{TiC}_2\text{T}_x$ (where Li et al. also approximated the effective carrier mass to the mass of an electron)^[45] but about two orders of magnitude lower than that of $\text{Ti}_3\text{C}_2\text{T}_x$ ^[31]. For this sample of Nb_2CT_x , the localization parameter, $c = -0.92 \pm 0.01$, is close to -1, suggesting that charge carriers are highly localized over distances comparable to their mean free path, either due to defects or edges of individual nanoflakes. As a result, static (or DC) conductivity can be estimated by extrapolating the real part of the Drude-Smith model out to 0 THz:

$$\sigma_{DC} = \text{Re}[\tilde{\sigma}(0)] = 62 \pm 15 \Omega^{-1} \text{cm}^{-1}. \quad (4)$$

We find that Nb_2CT_x has a low, but finite, intrinsic conductivity of $62 \pm 15 \Omega^{-1} \text{cm}^{-1}$, which is about two orders of magnitude lower than other MXenes like $\text{Ti}_3\text{C}_2\text{T}_x$ ^[31]. To corroborate this estimate of conductivity, we also measured this sample's conductivity using a four-point probe technique.^[80, 81] At $56 \pm 11 \Omega^{-1} \text{cm}^{-1}$, the DC conductivity measured was in good agreement with the THz measurement. Although this is low, it is still a measurable, nonzero quantity.

To understand the intrinsic conductivity, we calculate the intrinsic charge carrier mobility within individual nanoflakes from the Drude-Smith scattering time, τ_{DS} , as

$$\mu_{intrinsic} = \frac{e\tau_{DS}}{m^*}. \quad (5)$$

Again assuming $m^* = m_e$, and using $\tau_{DS} = 17 \pm 2 \text{ fs}$ from the Drude-Smith fit, we estimate the intrinsic carrier mobility of this sample to be $30 \pm 4 \text{ cm}^2 \text{ V}^{-1} \text{ s}^{-1}$. From here, we can estimate the long-range carrier mobility assuming,

$$\mu_{long-range} = \mu_{intrinsic}(1 + c), \quad (6)$$

which results in a long-range charge carrier mobility of $2.4 \pm 0.4 \text{ cm}^2 \text{ V}^{-1} \text{ s}^{-1}$. The significant disparity between intrinsic and long-range conductivities suggests – like in our previous work – that charge carrier mobility is impeded by the boundaries of the nanoflakes comprising our material.^[31, 45]

3.3 Time-resolved Terahertz Spectroscopy (TRTS)

Figures 4(a) and 4(b) both show the negative change in THz peak transmission following a 1.55 eV photoexcitation for three different fluences. As shown in Figure 3(c), the energy of this photoexcitation is quite close to the 1.7 eV plasmon resonance observed by Colin-Ulloa et. al. in Nb_2CT_x .^[33] In the limit of small changes ($-\Delta T/T < 20\%$), this is proportional to transient photoconductivity ($\Delta\sigma$). Figure 4(a) shows the early time window (within the first 10 ps after

photoexcitation, together with the photoexcited excess carrier densities, extracted from the Drude-Smith fits to transient photoconductivity spectra at different times after excitation, as discussed later), while Figure 4(b) displays normalized transient photoconductivity over an extended time window (as far out as 250 ps after photoexcitation). We find that photoexcitation of Nb_2CT_x results in a rapid onset of enhanced photoconductivity as interband excitations inject a new population of free carriers with the excess carrier density reaching $\sim 10\%$ of the intrinsic value.

Following this initial enhancement, the photoconductivity of the sample exhibits a significant decay within the first few ps (Fig. 4a). About 10 to 20 % of the photoinjected carriers have much longer lifetimes > 250 ps (Fig. 4b). The photoconductivity decays are clearly multi-exponential, revealing the presence of multiple relaxation channels. We find they can be well-described by three-component exponential decays, with decay times given in the inset to Fig. 4(b). All decay times increase with excitation fluence, a hallmark of saturation or filling of the channels responsible and ruling out carrier-carrier scattering or Auger recombination as candidates for the fastest, sub-ps decay. As proposed earlier for $\text{Nb}_4\text{C}_3\text{T}_x$, trapping on the fastest decay time can be attributed to defects arising from oxidation.^[32] They are presumably uniformly distributed throughout the nanosheets, allowing for fast trapping of excess carriers, and saturate with increasing injected excess carrier density. In addition to the most prominent, sub-ps decay, we observe a slightly slower decay time under 5 ps, which is followed by significantly longer decay times on the order of hundreds of ps. Those decays also show that the states responsible for the decays fill with increasing excitation fluence. We therefore ascribe them to carrier trapping at intra-nanosheet species as well as nanosheet edges.

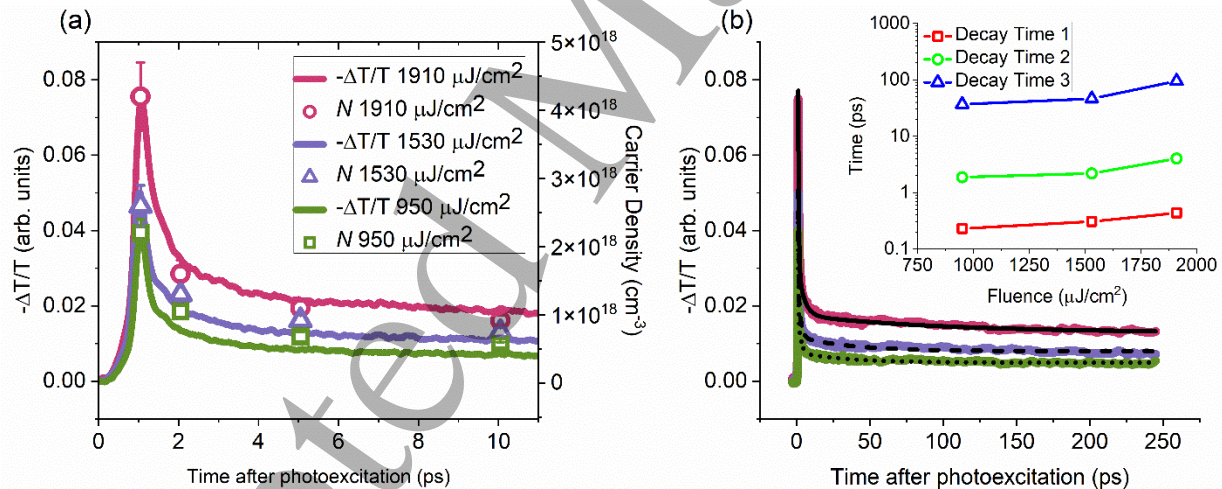


Figure 4. TRTS pump scans of Nb_2CT_x using three different photoexcitation fluences at 1.55eV. Each plot is fitted to a three-component exponential decay model, with solid, dashed, and dotted black lines corresponding to fluences of 950 $\mu\text{J}/\text{cm}^2$, 1530 $\mu\text{J}/\text{cm}^2$, and 1910 $\mu\text{J}/\text{cm}^2$, respectively. Panel (a) displays TRTS pump scans ranging from 1 ps before photoexcitation to 4 ps after, while panel (b) displays time range from 1 ps before photoexcitation to 250 ps after. Inset in (b) plots the three decay times on a semi-log plot a function of fluence. Error bars are too small to include for these decay times.

The enhancement in conductivity that we observe in Nb_2CT_x in response to photoexcitation is similar to the behavior of other MXenes including $\text{Mo}_2\text{Ti}_2\text{C}_3\text{T}_x$ ^[45], $\text{Mo}_2\text{TiC}_2\text{T}_x$ ^[45], and $\text{Nb}_4\text{C}_3\text{T}_x$ ^[32] but opposite to the negative photoconductivity seen in the highly conductive MXene, $\text{Ti}_3\text{C}_2\text{T}_x$ ^[31], where the dominant effect is heating of the intrinsic electron gas followed by a rapid increase in lattice temperature, which gives rise to a transiently reduced conductivity. In all these MXenes, both effects, injection of excess carriers and increase in carrier and lattice

temperature, are present, as photoexcitation quickly heats up the crystal lattice, as evidenced by the transient broadening of the plasmon resonance peak in $\text{Ti}_3\text{C}_2\text{T}_x$, $\text{Mo}_2\text{Ti}_2\text{C}_3\text{T}_x$ and Nb_2CT_x .^[33] Positive photoconductivity in $\text{Mo}_2\text{Ti}_2\text{C}_3\text{T}_x$, $\text{Mo}_2\text{TiC}_2\text{T}_x$ and Nb_2CT_x cannot be taken as the signature of semiconducting behavior. Rather, in metallic MXenes with sufficiently low intrinsic carrier density ($\leq 10^{20} \text{ cm}^{-3}$), transient increase in carrier density dominates over the transient decrease in carrier mobility.

To estimate the injected carrier density and gain additional information on their behavior, we extracted the complex, frequency-resolved photoconductivity at different points in the time (1 to 10 ps) after the sample has been photoexcited. Figure 5a, b and c, shows selected photoconductivity spectra at 1, 5, and 10 ps after photoexcitation for fluences of $1910 \mu\text{J}/\text{cm}^2$, respectively. Figure 5d, e and f plot the corresponding results for a fluence of $950 \mu\text{J}/\text{cm}^2$. Spectra at all 1, 2, 5, and 10 ps for all three fluence values studied are shown in Figure S2. Like in the case of intrinsic THz conductivity, the lines in Fig. 5 are the global fits of the real and imaginary photoconductivity components to the Drude-Smith model. From these fits, we can once again extract a localization parameter, scattering time, and carrier density for each spectrum.

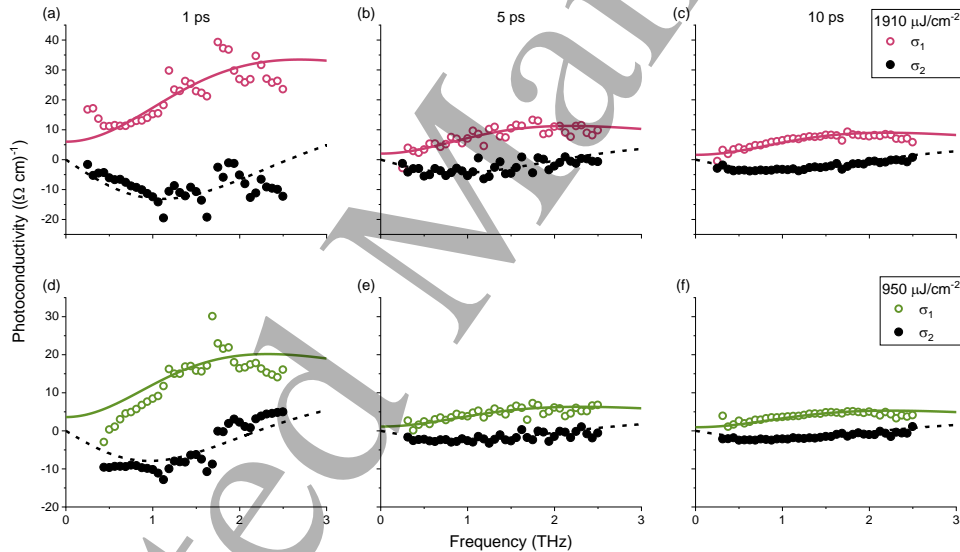


Figure 5. Photo-induced change in complex THz conductivity in Nb_2CT_x at 1, 5 and 10 ps after 1.55 eV photoexcitation with a), b) and c) fluences of $1910 \mu\text{J}/\text{cm}^2$ and (d) (e) and (f) $950 \mu\text{J}/\text{cm}^2$. Solid and dotted lines represent fits to the Drude-Smith model for complex conductivity.

Our measurements show that different fluences of 1.55 eV photoexcitations have little to no effect on the Drude-Smith parameters. We find that the localization parameter remains mostly unchanged after photoexcitation and remains that way for the first 10 ps thereafter, for all studied fluence values. The localization parameter was measured to be -0.91 ± 0.05 after photoexcitation, which is slightly lower than the $c = -0.92 \pm 0.01$, we measure in our TDS experiments. This suggests that the movement of photoexcited charge carriers in the material is suppressed to a similar degree as the movement of the intrinsic carriers.

On the other hand, we observe that the scattering time experienced by the carriers within at least the first 10 ps after excitation is significantly longer compared to the intrinsic carrier scattering time, $65 \pm 8 \text{ fs}$ vs. $17 \pm 2 \text{ fs}$, almost a

three-fold increase. An ultrashort pulse with average photon energy of 1.55 eV injects a population of hot free electrons (holes) into delocalized bands at the energies above (below) the Fermi level, and those excess carriers appear to experience a lower scattering rate and higher mobility. As in the case of the localization parameter, excitation fluence does not impact the carrier scattering time.

Finally, the Drude-Smith fitting of the experimental photoconductivity spectra at different times after excitation allows estimation of the photoexcited excess carrier density, plotted in Fig. 4(a) along with $-\Delta T/T$. We find that at the peak of measured photoconductivity, photoexcitation is responsible for a maximum excess carrier density of $(4.2 \pm 0.5) \times 10^{18} \text{ cm}^{-3}$, that is at most a few percent of the intrinsic carrier density.

Also, as the carrier mobility (determined by the scattering time and the localization parameter) is unchanged over the first 10 ps, we find that the transient photoconductivity decay is determined exclusively by the trapping and recombination of excess carriers. Based on the measured absorption coefficient at 1.55 eV ($5.6 \times 10^4 \text{ cm}^{-1}$, Figure 3(c)) and the penetration depth of $\sim 180 \text{ nm}$, comparable to the film thickness, neglecting reflection losses and assuming unity quantum efficiency, we estimate the upper limit of the injected carrier density to range from $\sim 3.9 \times 10^{20} \text{ cm}^{-3}$ for a fluence of $1910 \mu\text{J}/\text{cm}^2$ to $2.0 \times 10^{20} \text{ cm}^{-3}$ for a fluence of $950 \mu\text{J}/\text{cm}^2$, nearly two orders of magnitude higher than those experimentally observed at the peak of photoconductivity ($2.2 - 4 \times 10^{18} \text{ cm}^{-3}$, Fig. 4(a)). This suggests that most optically injected carriers are trapped and/or recombine due to fast nonlinear processes dominant at high carrier densities, such as Auger recombination, at times shorter than the experimental time resolution of $\sim 0.3 \text{ ps}$.

4. Summary

We have investigated the charge carrier transport mechanisms, as well as the electronic and optical properties of Nb_2CT_x MXene using a combination of DFT modeling of the electronic structure as a function of different surface terminations and THz spectroscopy. Through our combined DFT calculations and ultrafast optical spectroscopy measurements, we determine that this material is metallic for all surface terminations (apart from N) while also exhibiting increased carrier mobility, and consequently enhanced conductivity, when optically excited.

DFT calculations reveal that Nb_2CT_x has a metallic band structure (i.e., no band gap at E_F) for O, F, OH or mixed OH/F and O/OH terminations, independent of their ratios. Of the studied terminations, the only one that results in the opening of a band gap (0.71 eV) is the pure N-termination. Earlier reported XPS results do not show evidence of N terminations, thus predicting non-zero intrinsic free carrier density and metallic nature of Nb_2CT_x . In agreement with this prediction, THz-TDS measurements reveal an intrinsic carrier density of $(1.6 \pm 0.3) \times 10^{20} \text{ cm}^{-3}$ with carriers strongly localized due to disorder and nanoflake boundaries. Short-range, intraflake free carrier mobility is found to be $30 \pm 4 \text{ cm}^2 \text{ V}^{-1} \text{ s}^{-1}$, while the flake boundaries and disorder suppress the long-range (inter-flake) mobility to $2.4 \pm 0.4 \text{ cm}^2 \text{ V}^{-1} \text{ s}^{-1}$. Zero-frequency (DC) conductivity found by extrapolating the fit to the experimental THz conductivity, $62 \pm 15 \Omega^{-1} \text{ cm}^{-1}$, is in good agreement with our four-point probe measurements.

We also demonstrate that photoexcitation with 1.55 eV optical pump pulses result in a rapid enhancement in photoconductivity through a combination of inter-band injection of a new population of free charge carriers and intraband excitation of intrinsic carriers. Most of the photoinjected carriers recombine, within a few ps, but $\sim 10\text{-}20\%$

of photoinjected carriers persist for hundreds of ps. Rapid, over sub-ps, initial decay of photoinduced conductivity, where photoexcited carriers transfer energy to the crystal lattice, underlies the exceptionally efficient photothermal conversion efficiency that has been reported for this MXene. It can also be leveraged in high-speed photonic and optoelectronic devices.

Acknowledgements

Approved for public release by DEVCOM Soldier Center: PAO#PR2024-906. This work was supported in part by NSF DMR 2018326 and 1740795 awards and by the US Army DEVCOM Soldier Center AAI basic research program. AMF and ES acknowledge support from the NSF under the NRT-HDR-2021871 fellowship grant.

References

1. Naguib, M., et al., *Two-dimensional nanocrystals produced by exfoliation of Ti_3AlC_2* . *Advanced Materials*, 2011. **23**(37): p. 4248-4253.
2. Shahzad, F., et al., *Electromagnetic interference shielding with 2D transition metal carbides (MXenes)*. *Science*, 2016. **353**(6304): p. 1137-1140.
3. Rajavel, K., et al., *Investigation on the structural quality dependent electromagnetic interference shielding performance of few-layer and lamellar Nb_2CT_x MXene nanostructures*. *Journal of Alloys and Compounds*, 2021. **877**: p. 160235.
4. Hantanasirisakul, K. and Y. Gogotsi, *Electronic and optical properties of 2D transition metal carbides and nitrides (MXenes)*. *Advanced Materials*, 2018. **30**(52): p. 1804779.
5. Ghidui, M., et al., *Conductive two-dimensional Titanium Carbide 'clay' with high volumetric capacitance*. *Nature*, 2014. **516**(7529): p. 78-81.
6. Mashtalir, O., et al., *Intercalation and delamination of layered carbides and carbonitrides*. *Nature Communications*, 2013. **4**(1): p. 1716.
7. Dillon, A.D., et al., *Highly conductive optical quality solution-processed films of 2D Titanium Carbide*. *Advanced Functional Materials*, 2016. **26**(23): p. 4162-4168.
8. Naguib, M., et al., *New two-dimensional Niobium and Vanadium Carbides as promising materials for Li-Ion batteries*. *Journal of the American Chemical Society*, 2013. **135**(43): p. 15966-15969.
9. Eames, C. and M.S. Islam, *Ion intercalation into two-dimensional transition-metal carbides: global screening for new high-capacity battery materials*. *Journal of the American Chemical Society*, 2014. **136**(46): p. 16270-16276.
10. Liu, R., et al., *Nitrogen-doped Nb_2CT_x MXene as anode materials for lithium ion batteries*. *Journal of Alloys and Compounds*, 2019. **793**: p. 505-511.
11. Zhao, J., et al., *Nb_2CT_x MXene: high capacity and ultra-long cycle capability for lithium-ion battery by regulation of functional groups*. *Journal of Energy Chemistry*, 2021. **53**: p. 387-395.
12. Zhang, W., H. Jin, and J. Zhang, *Nb_2CT_x MXene as high-performance energy storage material with Na, K, and Liquid K-Na Alloy anodes*. *Langmuir*, 2021. **37**(3): p. 1102-1109.
13. Yuan, Z., et al., *Carbon-reinforced Nb_2CT_x MXene/ MoS_2 nanosheets as a superior rate and high-capacity anode for Sodium-ion batteries*. *ACS Nano*, 2021. **15**(4): p. 7439-7450.
14. Sarycheva, A., et al., *Two-Dimensional Titanium Carbide (MXene) as surface-enhanced raman scattering substrate*. *The Journal of Physical Chemistry C*, 2017. **121**(36): p. 19983-19988.

15. Chaudhuri, K., et al., *Highly broadband absorber using plasmonic Titanium Carbide (MXene)*. ACS Photonics, 2018. **5**(3): p. 1115-1122.
16. Velusamy, D.B., et al., *MXenes for plasmonic photodetection*. Advanced Materials, 2019. **31**(32): p. 1807658.
17. Montazeri, K., et al., *Beyond gold: spin-coated Ti_3C_2 -based MXene photodetectors*. Advanced Materials, 2019. **31**(43): p. 1903271.
18. Maleski, K., et al., *The broad chromatic range of two-dimensional transition metal carbides*. Advanced Optical Materials, 2021. **9**(4): p. 2001563.
19. Gao, L., et al., *Applications of few-layer Nb_2C MXene: narrow-band photodetectors and femtosecond mode-locked fiber lasers*. ACS Nano, 2021. **15**(1): p. 954-965.
20. Li, G., et al., *Third-order nonlinear optical response of few-layer MXene Nb_2C and applications for square-wave laser pulse generation*. Advanced Materials Interfaces, 2021. **8**(6): p. 2001805.
21. Kumar, A.N. and K. Pal, *Amine-functionalized stable Nb_2CT_x MXene toward room temperature ultrasensitive NO_2 gas sensor*. Materials Advances, 2022. **3**(12): p. 5151-5162.
22. Shabana, N., et al., *In-situ decoration of Platinum nanoparticles on Nb_2CT_x MXene: an electrochemical sensor for L-Cysteine and an efficient catalyst for oxygen evolution reaction*. ECS Journal of Solid State Science and Technology, 2022. **11**(12): p. 127002.
23. Lin, H., et al., *A two-dimensional biodegradable Niobium Carbide (MXene) for photothermal tumor eradication in NIR-I and NIR-II biowindows*. Journal of the American Chemical Society, 2017. **139**(45): p. 16235-16247.
24. Han, X., et al., *Therapeutic mesopore construction on 2D Nb_2C MXenes for targeted and enhanced chemo-photothermal cancer therapy in NIR-II biowindow*. Theranostics, 2018. **8**(16): p. 4491-4508.
25. Xuan, J., et al., *Organic-base-driven intercalation and delamination for the production of functionalized Titanium Carbide nanosheets with superior photothermal therapeutic performance*. Angewandte Chemie International Edition, 2016. **55**(47): p. 14569-14574.
26. Dai, C., et al., *Two-dimensional Tantalum Carbide (MXenes) composite nanosheets for multiple imaging-guided photothermal tumor ablation*. ACS Nano, 2017. **11**(12): p. 12696-12712.
27. Li, R., et al., *MXene Ti_3C_2 : an effective 2D light-to-heat conversion material*. ACS Nano, 2017. **11**(4): p. 3752-3759.
28. Zhao, Y., et al., *Photocatalytic sterilization performance and mechanism of pure Nb_2CT_x MXenes nanosheets under infrared light irradiation*. Applied Surface Science, 2023. **613**: p. 155990.
29. Chen, J., et al., *Tailored hydrogel delivering Niobium Carbide boosts ROS-scavenging and antimicrobial activities for diabetic wound healing*. Small, 2022. **18**(27): p. 2201300.
30. Wang, Y., et al., *2D Nb_2CT_x MXene/ MoS_2 heterostructure construction for nonlinear optical absorption modulation*. Opto-Electronic Advances, 2023. **6**(10): p. 220162-1-220162-11.
31. Li, G., et al., *Equilibrium and non-equilibrium free carrier dynamics in 2D $Ti_3C_2T_x$ MXenes: THz spectroscopy study*. 2D Materials, 2018. **5**(3): p. 035043.
32. Zheng, W., et al., *Band transport by large Fröhlich polarons in MXenes*. Nature Physics, 2022. **18**: p. 544 - 550.
33. Colín-Ulloa, E., et al., *Ultrafast spectroscopy of plasmons and free carriers in 2D MXenes*. Advanced Materials, 2023. **35**(8): p. 2208659.
34. Huang, Y., et al., *Abnormally strong electron-phonon scattering induced unprecedented reduction in lattice thermal conductivity of two-dimensional Nb_2C* . Journal of the American Chemical Society, 2019. **141**(21): p. 8503-8508.
35. Shao, Y., et al., *N-functionalized MXenes: ultrahigh carrier mobility and multifunctional properties*. Physical Chemistry Chemical Physics, 2017. **19**(42): p. 28710-28717.
36. Gao, L., et al., *Ultrafast relaxation dynamics and nonlinear response of few-layer Niobium Carbide MXene*. Small Methods, 2020. **4**(8): p. 2000250.

- 1
2
3 37. Natu, V., et al., *Effect of base/nucleophile treatment on interlayer ion intercalation, surface terminations, and osmotic swelling of $Ti_3C_2T_z$ MXene multilayers*. Chemistry of Materials, 2022. **34**(2): p. 678-693.
- 4
5
6 38. Natu, V. and M.W. Barsoum, *MXene surface terminations: a perspective*. The Journal of Physical Chemistry C, 2023. **127**(41): p. 20197-20206.
- 7
8 39. Li, Y., et al., *A general Lewis acidic etching route for preparing MXenes with enhanced electrochemical performance in non-aqueous electrolyte*. Nature Materials, 2020. **19**(8): p. 894-899.
- 9
10
11 40. Arole, K., et al., *Exfoliation, delamination, and oxidation stability of molten salt etched Nb_2CT_z MXene nanosheets*. Chemical Communications, 2022. **58**(73): p. 10202-10205.
- 12
13 41. Liu, L., et al., *Exfoliation and delamination of $Ti_3C_2T_x$ MXene prepared via molten salt etching route*. ACS Nano, 2022. **16**(1): p. 111-118.
- 14
15 42. Kamysbayev, V., et al., *Covalent surface modifications and superconductivity of two-dimensional metal carbide MXenes*. Science, 2020. **369**(6506): p. 979-983.
- 16
17 43. Bai, Y., et al., *MXene-Copper/Cobalt hybrids via Lewis acidic molten salts etching for high performance symmetric supercapacitors*. Angewandte Chemie International Edition, 2021. **60**(48): p. 25318-25322.
- 18
19 44. Li, G., et al., *Dynamical control over terahertz electromagnetic interference shielding with 2D $Ti_3C_2T_y$ MXene by ultrafast optical pulses*. Nano Letters, 2020. **20**(1): p. 636-643.
- 20
21 45. Li, G., et al., *Two-dimensional MXenes $Mo_2Ti_2C_3T_z$ and $Mo_2TiC_2T_z$: microscopic conductivity and dynamics of photoexcited carriers*. ACS Applied Energy Materials, 2020. **3**(2): p. 1530-1539.
- 22
23 46. Li, E., et al., *Charge carriers localization effect revealed through terahertz spectroscopy of MXene: $Ti_3C_2T_x$* . Small, 2023: p. 2306200.
- 24
25 47. Kresse, G. and J. Hafner, *Ab initio molecular-dynamics simulation of the liquid-metal--amorphous-semiconductor transition in Germanium*. Physical Review B, 1994. **49**(20): p. 14251-14269.
- 26
27 48. Kresse, G. and J. Hafner, *Ab initio molecular dynamics for liquid metals*. Physical Review B, 1993. **47**(1): p. 558-561.
- 28
29 49. Kresse, G. and J. Furthmüller, *Efficient iterative schemes for ab initio total-energy calculations using a plane-wave basis set*. Physical Review B, 1996. **54**(16): p. 11169-11186.
- 30
31 50. Kresse, G. and J. Furthmüller, *Efficiency of ab-initio total energy calculations for metals and semiconductors using a plane-wave basis set*. Computational Materials Science, 1996. **6**(1): p. 15-50.
- 32
33 51. Perdew, J.P., K. Burke, and M. Ernzerhof, *Generalized gradient approximation made simple*. Physical Review Letters, 1996. **77**(18): p. 3865-3868.
- 34
35 52. Blöchl, P.E., *Projector augmented-wave method*. Physical Review B, 1994. **50**(24): p. 17953-17979.
- 36
37 53. Kresse, G. and D. Joubert, *From ultrasoft pseudopotentials to the projector augmented-wave method*. Physical Review B, 1999. **59**(3): p. 1758-1775.
- 38
39 54. Heyd, J., G.E. Scuseria, and M. Ernzerhof, *Hybrid functionals based on a screened Coulomb potential*. The Journal of Chemical Physics, 2003. **118**(18): p. 8207-8215.
- 40
41 55. Wang, V., et al., *VASPKIT: a user-friendly interface facilitating high-throughput computing and analysis using VASP code*. Computer Physics Communications, 2021. **267**: p. 108033.
- 42
43 56. VahidMohammadi, A., J. Rosen, and Y. Gogotsi, *The world of two-dimensional carbides and nitrides (MXenes)*. Science, 2021. **372**(6547): p. eabf1581.
- 44
45 57. Caffrey, N.M., *Effect of mixed surface terminations on the structural and electrochemical properties of two-dimensional $Ti_3C_2T_2$ and V_2CT_2 MXenes multilayers*. Nanoscale, 2018. **10**(28): p. 13520-13530.
- 46
47 58. Wang, X., et al., *Atomic-scale recognition of surface structure and intercalation mechanism of Ti_3C_2X* . Journal of the American Chemical Society, 2015. **137**(7): p. 2715-2721.
- 48
49
50
51
52
53
54
55
56
57
58
59
60

- 1
2
3 59. Zha, X.-H., et al., *Role of the surface effect on the structural, electronic and mechanical*
4 *properties of the carbide MXenes*. Europhysics Letters, 2015. **111**(2): p. 26007.
- 5 60. Hu, J., et al., *Investigations on Nb₂C monolayer as promising anode material for Li or non-Li ion*
6 *batteries from first-principles calculations*. RSC Advances, 2016. **6**(33): p. 27467-27474.
- 7 61. Jepsen, P.U., D.G. Cooke, and M. Koch, *Terahertz spectroscopy and imaging – Modern*
8 *techniques and applications*. Laser & Photonics Reviews, 2011. **5**(1): p. 124-166.
- 9 62. Cocker, T.L., et al., *Terahertz conductivity of the metal-insulator transition in a nanogranular*
10 *VO₂ film*. Applied Physics Letters, 2010. **97**(22).
- 11 63. Baxter, J.B. and C.A. Schmuttenmaer, *Carrier dynamics in bulk ZnO. I. Intrinsic conductivity*
12 *measured by terahertz time-domain spectroscopy*. Physical Review B, 2009. **80**(23): p. 235205.
- 13 64. Cooke, D.G., *Terahertz photoconductivity*, in *Photoconductivity and Photoconductive Materials*.
14 2022. p. 369-398.
- 15 65. Neu, J. and C.A. Schmuttenmaer, *Tutorial: an introduction to terahertz time domain spectroscopy*
16 *(THz-TDS)*. Journal of Applied Physics, 2018. **124**(23).
- 17 66. Ulbricht, R., et al., *Carrier dynamics in semiconductors studied with time-resolved terahertz*
18 *spectroscopy*. Reviews of Modern Physics, 2011. **83**(2): p. 543-586.
- 19 67. Butler, K.T., et al., *Ultrafast carrier dynamics in BiVO₄ thin film photoanode material: interplay*
20 *between free carriers, trapped carriers and low-frequency lattice vibrations*. Journal of Materials
21 Chemistry A, 2016. **4**(47): p. 18516-18523.
- 22 68. Titova, L.V., et al., *Ultrafast carrier dynamics and the role of grain boundaries in polycrystalline*
23 *silicon thin films grown by molecular beam epitaxy*. Semiconductor Science and Technology,
24 2016. **31**(10): p. 105017.
- 25 69. Lloyd-Hughes, J. and T.-I. Jeon, *A review of the terahertz conductivity of bulk and nano-*
26 *materials*. Journal of Infrared, Millimeter, and Terahertz Waves, 2012. **33**(9): p. 871-925.
- 27 70. Yang, Y. and C.S. Ting, *Electronic structures and electron-phonon superconductivity of Nb₂C-*
28 *based MXenes*. Journal of Physics D: Applied Physics, 2020. **53**(48): p. 485301.
- 29 71. Khazaei, M., et al., *Novel electronic and magnetic properties of two-dimensional transition metal*
30 *carbides and nitrides*. Advanced Functional Materials, 2013. **23**(17): p. 2185-2192.
- 31 72. Yusupov, K., J. Björk, and J. Rosen, *A systematic study of work function and electronic properties*
32 *of MXenes from first principles*. Nanoscale Advances, 2023. **5**(15): p. 3976-3984.
- 33 73. Shao, Y., *MXene-Based Materials for Energy Conversion/Storage and Device Applications: A*
34 *First-Principles Study*. 2020, University of Macau: Peoples Rep. of China. p. 164.
- 35 74. Grischkowsky, D., et al., *Far-infrared time-domain spectroscopy with terahertz beams of*
36 *dielectrics and semiconductors*. Journal of the Optical Society of America B, 1990. **7**(10): p.
37 2006-2015.
- 38 75. Naftaly, M. and R.E. Miles, *Terahertz time-domain spectroscopy for material characterization*.
39 *Proceedings of the IEEE*, 2007. **95**: p. 1658-1665.
- 40 76. Richter, C. and C.A. Schmuttenmaer, *Exciton-like trap states limit electron mobility in TiO₂*
41 *nanotubes*. Nature Nanotechnology, 2010. **5**(11): p. 769-772.
- 42 77. Alberding, B.G., et al., *Static and time-resolved terahertz measurements of photoconductivity in*
43 *solution-deposited Ruthenium Dioxide nanofilms*. J Phys Chem C Nanomater Interfaces, 2017.
44 **121**(7): p. 4037-4044.
- 45 78. Walther, M., et al., *Terahertz conductivity of thin gold films at the metal-insulator percolation*
46 *transition*. Physical Review B, 2007. **76**(12): p. 125408.
- 47 79. Smith, N.V., *Classical generalization of the Drude formula for the optical conductivity*. Physical
48 Review B, 2001. **64**(15): p. 155106.
- 49 80. Valdes, L.B., *Resistivity measurements on Germanium for transistors*. Proceedings of the IRE,
50 1954. **42**(2): p. 420-427.
- 51 81. Smits, F.M., *Measurement of sheet resistivities with the four-point probe*. The Bell System
52 Technical Journal, 1958. **37**(3): p. 711-718.
- 53
54
55
56
57
58
59
60

1
2
3
4
5
6
7
8
9
10
11
12
13
14
15
16
17
18
19
20
21
22
23
24
25
26
27
28
29
30
31
32
33
34
35
36
37
38
39
40
41
42
43
44
45
46
47
48
49
50
51
52
53
54
55
56
57
58
59
60

Accepted Manuscript